Magnetic-Field-Induced Quantum Phase Transitions in a van der Waals Magnet

Siwen Li,[1] Zhipeng Ye,[2] Xiangpeng Luo,[1] Gaihua Ye,[2] Hyun Ho Kim,[3] Bowen Yang,[3] Shangjie Tian,[4] Chenghe Li,[4] Hechang Lei,[4] Adam W. Tsen,[3] Kai Sun,[1] Rui He[2,*] and Liuyan Zhao[1,†]

[1]*Department of Physics, University of Michigan, 450 Church Street, Ann Arbor, Michigan 48109, USA*
[2]*Department of Electrical and Computer Engineering, Texas Tech University,*
910 Boston Avenue, Lubbock, Texas 79409, USA
[3]*Institute for Quantum Computing, Department of Chemistry, and Department of Physics and Astronomy,*
University of Waterloo, Waterloo, 200 University Avenue W, Ontario N2L 3G1, Canada
[4]*Department of Physics and Beijing Key Laboratory of Opto-electronic Functional Materials &*
Micro-nano Devices, Remin University of China, Beijing 100872, China

Exploring new parameter regimes to realize and control novel phases of matter has been a main theme in modern condensed matter physics research. The recent discovery of two-dimensional (2D) magnetism in nearly freestanding monolayer atomic crystals has already led to observations of a number of novel magnetic phenomena absent in bulk counterparts. Such intricate interplays between magnetism and crystalline structures provide ample opportunities for exploring quantum phase transitions in this new 2D parameter regime. Here, using magnetic field- and temperature-dependent circularly polarized Raman spectroscopy of phonons and magnons, we map out the phase diagram of chromium triiodide (CrI_3) that has been known to be a layered antiferromagnet (AFM) in its 2D films and a ferromagnet (FM) in its three-dimensional (3D) bulk. However, we reveal a novel mixed state of layered AFM and FM in 3D CrI_3 bulk crystals where the layered AFM survives in the surface layers, and the FM appears in deeper bulk layers. We then show that the surface-layered AFM transits into the FM at a critical magnetic field of 2 T, similar to what was found in the few-layer case. Interestingly, concurrent with this magnetic phase transition, we discover a first-order structural phase transition that alters the crystallographic point group from C_{3i} (rhombohedral) to C_{2h} (monoclinic). Our result not only unveils the complex single-magnon behavior in 3D CrI_3, but it also settles the puzzle of how CrI_3 transits from a bulk FM to a thin-layered AFM semiconductor, despite recent efforts in understanding the origin of layered AFM in CrI_3 thin layers, and reveals the intimate relationship between the layered AFM-to-FM and the crystalline rhombohedral-to-monoclinic phase transitions. These findings further open opportunities for future 2D magnet-based magnetomechanical devices.

Subject Areas: Condensed Matter Physics

I. INTRODUCTION

Chromium triiodide (CrI_3) stands out among the large family of van der Waals (VDW) ferromagnets (FMs) investigated so far, because its isolated atomic crystal is one of the first two to realize two-dimensional (2D) ferromagnetic long-range order [1,2] in the monolayer limit, and more importantly, it is the first-ever interlayer

*Corresponding author.
rui.he@ttu.edu
†Corresponding author.
lyzhao@umich.edu

antiferromagnetic (AFM) semiconductor [3–6] in its multilayer form. This phenomenon also makes CrI_3 distinct from the 2D intralayer AFMs [7–9]. From an application perspective, such unique magnetic properties of CrI_3 have already drawn enormous interest in developing novel device functionalities that are tunable by either magnetic [3–6] or electric [10–12] fields. From a fundamental science point of view, extensive static and dynamic measurements in both three-dimensional (3D) bulk [13,14] and 2D film [3–6,15,16] CrI_3 have been performed to understand the mechanism of the magnetism that has remained elusive until now. Our study here approaches the nature of CrI_3 magnetism through exploring the magnetic field dependence of spin-wave excitations in CrI_3 and interrogating the interplay between the magnetic order and the crystalline structure.

In its bulk form, CrI_3 goes through a monoclinic (C_{2h}) to rhombohedral (C_{3i}) structural phase transition at

$T_s = 220$ K and develops a FM long-range order at $T_{\text{FM}} = 61$ K [13]. Across T_s, the major structural change involves the shearing of the VDW bonded CrI_3 layers of the honeycomb lattice from a tilted to an aligned ABC stacking sequence [13]. Below T_{FM}, all the spin moments within and between layers align along the out-of-plane direction [13], and a spin-wave gap of approximately 1 meV emerges at the Brillouin-zone-center Γ point as a result of the Ising-type exchange anisotropy [14]. The magnetic and crystallographic degrees of freedom couple strongly in bulk CrI_3 as evidenced by the enhanced reduction of interlayer spacing below T_{FM} [13]. In its thin-layer form, the CrI_3 magnetism is known to survive below $T_{\text{AFM}} = 45$ K; however, in a unique layered AFM order in which spins align along the same out-of-plane direction within each layer and alternate to the opposite orientation between adjacent layers [3–6], while its crystal structure is much less studied experimentally. The origin of this crossover from the FM in bulk to the layered AFM in thin films, as well as the role of the crystallographic structure in this transition, remains as outstanding open question in the field of 2D magnetism.

II. EXPERIMENT AND ANALYSIS

In order to probe both the magnetic and crystallographic degrees of freedom in CrI_3, we carry out polarized Raman spectroscopy to detect the symmetry-resolved collective excitations of spin precessions (i.e., magnons) [17] and lattice vibrations (i.e., phonons) [18–21], respectively. To further reveal the interplay between these 2 degrees of freedom, we perform both temperature- and magnetic field-dependent Raman measurements covering a temperature (T) range from room temperature down to 10 K and a magnetic field (B) range from 0 up to 7 T. Because the stray magnetic fields cause the Faraday rotation of linearly polarized light transmitted through the objective in close proximity to the magnet [22], we choose circularly polarized light to perform reliable selection rule measurements (see the Supplemental Material Sec. 1 [23] for Raman selection rules in the circular polarization basis for CrI_3, and see Methods for details of the Raman measurements).

A. Magnetism-related Raman modes

We start by showing Raman spectra in both parallel and crossed circularly polarized channels labeled as LL and LR in Fig. 1(a), respectively, taken on a freshly cleaved 3D CrI_3 crystal at $T = 10$ K and $B = 0$ T, where LL(R) stands for incident and scattered light being left and left (right) circularly polarized, respectively. We categorize all the observable Raman modes into three categories based on their symmetry properties. The first category contains phonon modes of either A_g or E_g symmetry of the C_{3i} point group as reported before using linearly polarized light [15,24,25]. Under the circular polarization basis in Fig. 1(a),

the A_g phonon modes [labeled $P(A_g)$] appear only in the LL channel, and the E_g ones [$P(E_g)$] are solely in the LR channel, as expected for the rhombohedral crystal structure. The second group consists of two modes M_1 and M_2 that were previously shown to be antisymmetric and attributed to surface magnetic excitations [15], showing up in the LL channel here. The third kind is exclusively very low-frequency modes M_0 that, however, have neither been detected experimentally [15,24,25] nor predicted theoretically [26,27] before in Raman studies and are present in both LL and LR channels. Symmetrywise, these M_0-type modes violate the selection rules for the rhombohedral crystal structure and the FM order. Energywise, their frequencies of approximately 4 cm^{-1} (0.49 meV) are close to the reported bulk spin-wave gap, which is on the order of 1 meV [14]. We note that the M_0 intensity is stronger in the anti-Stokes than the Stokes channel, possibly due to the resonance excitation to the charge-transfer transition in CrI_3 and the broken time-reversal symmetry of M_0.

To explore the nature of these potentially magnetism-related Raman modes M_{0-2} and investigate the magnetoe-lastic coupling between magnetic and phononic modes, we carefully carry out out-of-plane magnetic field- ($B \perp ab$) dependent Raman measurements at 10 K and show the results in the LL channel in Fig. 1(b) (see Supplemental Material Sec. 2 [23] for extended data of magnetic field-dependent Raman spectra on 3D CrI_3 bulk). First of all, it is clear that the frequencies of M_0 scale linearly with the magnetic field, consistent with what would be expected for spin-wave excitations, despite a discontinuity at approximately 2 T and a much more complex pattern for the magnetic fields lower than 2 T. In addition, at 0 T, M_0-type modes soften toward 0 cm^{-1} when approaching the critical temperature T_c of 45 K from below, which is consistent with the expected trend of $\sqrt{T_c - T}$ for an order parameter under the mean-field theory [28,29] [Fig. 1(d) top panel]. Based on both the linear magnetic field dependence and the softening of M_0 frequencies, we confidently assign M_0-type modes to be spin-wave excitations. Second, the M_1 and M_2 show no magnetic field dependence at all below 2 T and disappear at higher magnetic fields. Although their antisymmetric selection rule is indicative of their magnetic origin [17] and their temperature-dependent intensities mimic closely that of the magnetic order parameter [28,29] [Fig. 1(d) middle and bottom panels], such a magnetic field independence of M_1 and M_2 before 2 T immediately rules out the possibility of them being conventional spin-wave excitations. More insights about their potential nature are discussed later in Fig. 2. Third, the phonons exhibit contrasting selection rules below and above 2 T while their frequencies remain more or less independent of magnetic field. For example, the E_g mode (at approximately 109 cm^{-1}) leaks into the LL channel [Fig. 1(b)], and the A_g modes (at approximately 79 and 129 cm^{-1}) show up in the LR channel above 2 T (see Supplemental Material Sec. 2 [23]).
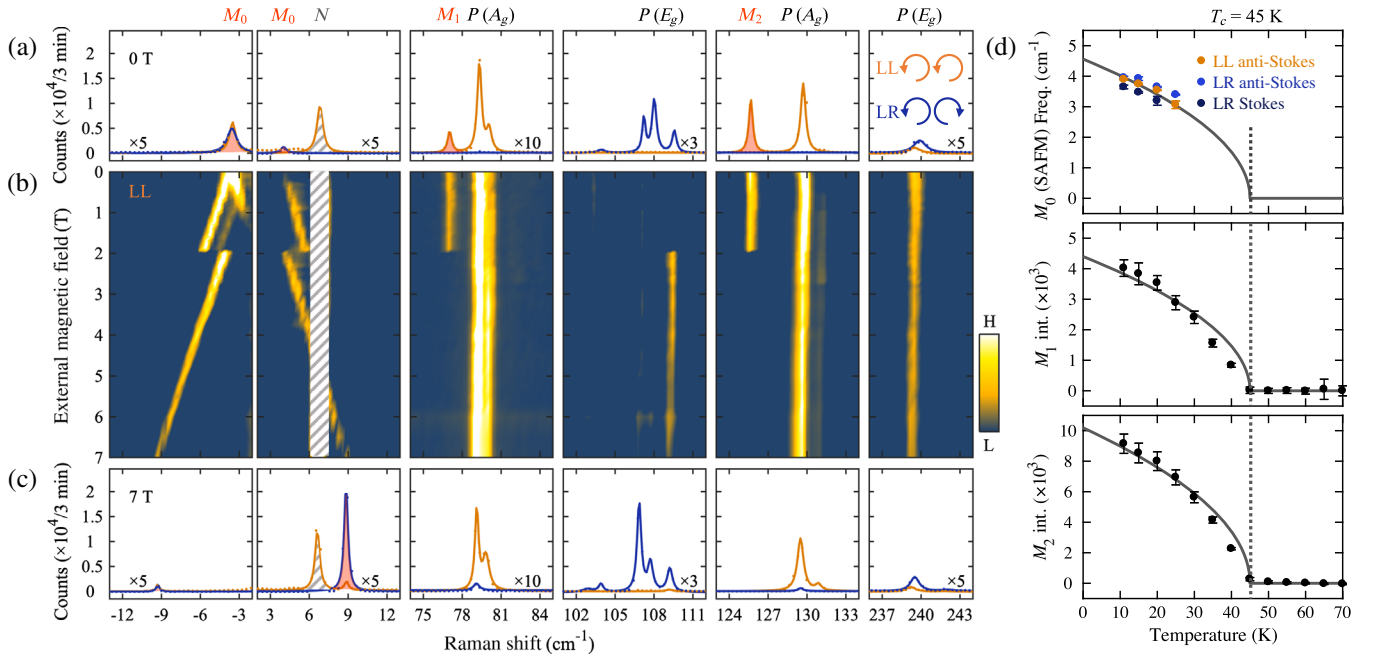
FIG. 1.   Identifying the magnetism-related Raman modes in 3D CrI$_3$. (a) Raman spectra taken at 10 K and 0 T in the LL and LR channels. LL(R) stands for the polarization channel in which the incident and scattered light is left and left (right) circularly polarized, respectively. Solid dots are raw data points and solid lines are Lorentzian fits. The multiplication factors to the spectra intensities are labeled in the corresponding panels. The Raman modes are labeled as $M_{0,1,2}$ for the magnetism-related ones (shaded in orange), $P(A_g)$ and $P(E_g)$ for the phonon modes of the A_g and E_g symmetries of the C_{3i} point group, respectively, and N for the noise line from the incident light (shaded in gray stripes). Inset shows the legends for the polarization channels. (b) A color map of magnetic field-dependent Raman spectra taken over a magnetic field range of 0–7 T at 10 K in the LL channel. The gray stripe-patterned shade is to block the noise line. (c) Raman spectra taken at 10 K and 7 T in the LL and LR channels. (d) Temperature dependence of the M_0 frequency (including data for the LL anti-Stokes, LR anti-Stokes, and Stokes shifts) and $M_{1,2}$ intensities at zero magnetic field ($B = 0$ T) showing a clear onset at T_c of 45 K. Error bars are defined as one standard error of the fitting parameters in the Lorentzian fit to the Raman modes.

Having described the Raman spectra evolution with increasing magnetic field, we show in Fig. 1(c) both Raman spectra in the LL and LR channels at our highest available magnetic field of 7 T. Comparing to the spectra taken at 0 T in Fig. 1(a), one of the M_0 modes shifts up to nearly 9 cm^{-1} with its spectral intensity primarily in the LR channel, while neither M_1 nor M_2 are present in either the LR or LL channel. In addition, observable fractions of phonon intensities leak into the corresponding orthogonal channels, suggesting that the crystalline symmetry is lowered from the C_{3i} point group at 0 T. So far, we establish that both the magnetic order and the crystalline structure change across a critical magnetic field B_c of about 2 T. To gain more insight into these magnetic-field-induced phase transitions and their relationships to one the other, in the following, we first discuss the magnetic phase transition from the magnetic field dependence of M_0 and then address the structural phase transition from the combination of the magnetic field dependence of the M_{1-2}, A_g, and E_g phonons.

B. Zeeman shift of spin waves

To provide a comprehensive picture of the magnetic field dependence of M_0, we summarize in Fig. 2(a) the key

experimental result of the M_0 frequencies shifting as a function of the external magnetic field and the corresponding field-dependent spin-wave calculations in the left and right panels, respectively. Here, we show the average M_0-type mode frequencies from the Lorentzian fit of the Raman spectra for both the Stokes and anti-Stokes shift in both the LL and LR channels. Strikingly, despite the fact that bulk CrI$_3$ is considered as a simple Ising ferromagnet [13], we observe that three spin-wave branches at magnetic fields lower than 2 T collapse into one across $B_c = 2$ T. In particular, a pair of the three branches below 2 T start with close frequencies of approximately 3.4 and 3.9 cm^{-1} at 0 T and evolve in opposite trends at increasing magnetic field (M_{0a} and M_{0b}), while the third one increases linearly since its appearance at approximately 1 T and continues after B_c of 2 T with a weak discontinuity of frequency redshift (M_{0c}). The field dependence of M_{0a} and M_{0b} is typical behavior of spin waves in AFMs in which the angular momenta of two degenerate spin waves align parallel and antiparallel, respectively, to the external magnetic field, and M_{0c} is consistent with spin waves in FMs.

Our experimental observations above suggest a mixed state of layered AFM and FM for a 3D CrI$_3$ bulk, in contrast to the literature assignment of a pure FM
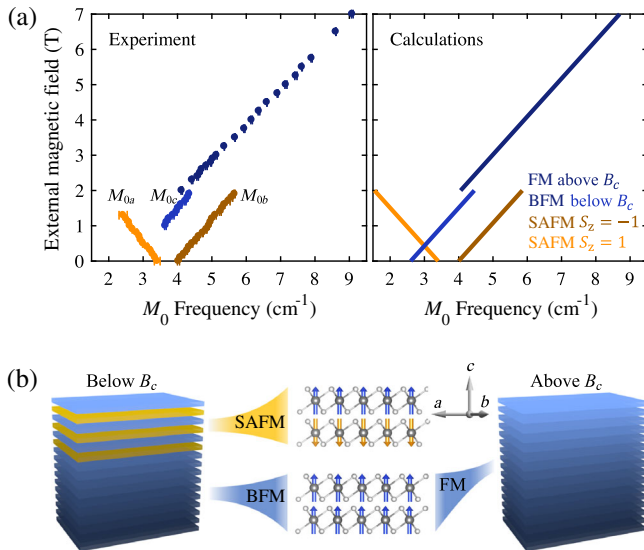
FIG. 2. Establishing the mixed SAFM and BFM phase in 3D CrI$_3$. (a) Experimental data (left) and spin-wave calculations (right) for the magnetic field dependence of M_0-type mode frequencies. M_{0a}, M_{0b}, and M_{0c} label the three spin-wave branches below the critical magnetic field B_c of 2 T. Error bars correspond to one standard error of the fitted central frequencies for the M_0-type Raman modes and are mostly smaller than the data point symbols. (b) Schematic illustration of the mixed state of the surface-layered AFM (SAFM for the state with alternating spin moments in the adjacent layers) and the deep bulk FM (BFM for the state with all the spin moments along one direction) below B_c and the pure FM state above B_c.

phase [13]. This suggestion is consistent with the absence of M_{0c} below B_c in CrI$_3$ flakes (see Supplemental Material Sec. 3 [23]). As sketched in Fig. 2(b), below B_c, top layers of bulk CrI$_3$ show layered AFM (denoted as SAFM) that is similar to what has been reported in 2D CrI$_3$ thin films [3–6], and deeper bulk exhibits a FM order (denoted as BFM) that is consistent with what bulk magnetization measurements find [30]. The small energy scale of about 1 μeV [31] of the long-range magnetic dipole-dipole interactions that favor the interlayer FM is much weaker than the interlayer AFM exchange coupling of 150 μeV. Therefore, we rule out the possibility of pure magnetic energetic reasons and require surface reconstructions to establish the interlayer AFM coupling at the surface while having FM coupling in the bulk. Hence, the SAFM provides the pair of spin waves with opposite Zeeman shifts (M_{0a} and M_{0b}) while the BFM leads to the third branch with a linearly increasing frequency with growing magnetic field (M_{0c}). Also noted is that the BFM provides an effective magnetic field of 0.27 T to lift the degeneracy of two spin waves of the SAFM at the 0-T external magnetic field. Above B_c, SAFM transits into FM in the same manner as layered AFM in CrI$_3$ thin flakes [3–6], leading the entire CrI$_3$ crystal into a FM state as shown in Fig. 2(b) and resulting in a sole spin-wave branch above B_c.

This SAFM-to-FM transition in 3D CrI$_3$ bulk is further supported by a weak anomaly at $B_c = \pm 2$ T in the magnetization vs magnetic field measurements (see Supplemental Material Sec. 4 [23]). Based on this proposed model, the calculated magnetic field dependence of the M_0-type mode frequencies [right, Fig. 2(a) with a nearest-neighbor Ising spin Hamiltonian coincides well with our experimental data [left, Fig. 2(a)] (see the calculation details in Supplemental Material Sec. 5 [23]). Based on the selection rule for M_0 evolving from the nearly equal weighted presence in both LL and LR channels at 0 T to a dominant selection in the LR channel at 7 T, we can further infer that the spin moments in CrI$_3$ orient from being tilted away to nearly aligned with the surface normal as the external magnetic field increases.

C. Structural phase transition

Concurrent with the magnetic phase transition at B_c, we also observe an evident first-order structural phase transition manifested by abrupt changes in phonons [Figs. 3(a)–3(d)]. First and foremost, the appearance of fully symmetric A_g phonons in the LR channel [Fig. 3(a)] reveals the transformation of their Raman tensors from the $\begin{pmatrix} a & \cdot \\ \cdot & a \end{pmatrix}$ to the $\begin{pmatrix} a & \cdot \\ \cdot & b \end{pmatrix}$ form, suggesting the loss of the threefold rotational symmetry and thus the breaking of the rhombohedral crystal symmetry. We propose the shearing of VDW layers away from the aligned ABC stacking order [Fig. 3(e)], which is indeed a structural instability for CrI$_3$ bulk [13,32], as one means to transit from the C_{3i} rhombohedral (nearly D_{3d} because of weak interlayer interactions) to the C_{2h} monoclinic crystal symmetry (see Supplemental Material Sec. 1 [23] for C_{2h} Raman selection rules and Sec. 6 for its comparison to the high-temperature monoclinic structure). Interestingly, this magnetic-field-induced monoclinic phase mimics a 3D quantum nematic long-range order with a director as its order parameter which breaks the rotational symmetry but preserves the lattice translational symmetry [indicated as elongated ellipses in Fig. 3(e)]. It is known that such a 3D quantum nematic order must emerge through the first-order phase transition [33], as is indeed our case here. Second, for the E_g phonons, which are present only in the LR channel below B_c, some of their intensities exhibit leakage into the LL channel right across B_c while some others show clear jumps in the LR channel at B_c without leaking into the LL channel [examples of each case are shown in Figs. 3(b) and 3(c)]. These two cases are consistent with the $E_g(C_{3i})$ phonons transforming into the $A_g(C_{2h})$ and $B_g(C_{2h})$ phonons, respectively, which further corroborates the proposed structural phase transition at B_c. Third, the antisymmetric $M_{1,2}$ modes stay nearly constant until B_c and disappear right above B_c [see M_2 in Fig. 3(d) and M_1 in Supplemental Material Sec. 7 [23]]. Both modes were initially interpreted as surface magnetic excitations based
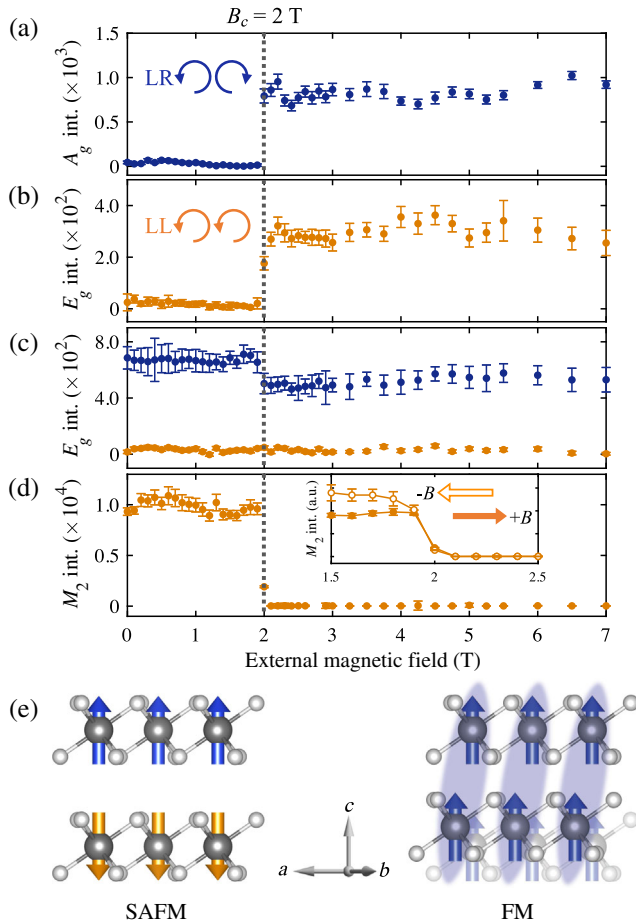
FIG. 3. Revealing the rhombohedral-to-monoclinic structural phase transition at B_c in 3D CrI_3. Magnetic field dependence of (a) a representative A_g phonon (at approximately 129 cm^{-1}) intensity leakage into the LR channel, (b) an example of an E_g phonon (at approximately 109 cm^{-1}) intensity showing up in the LL channel, which corresponds to the E_g phonon of the C_{3i} structure [i.e., $E_g(C_{3i})$] transforming into the A_g phonon of the C_{2h} structure [i.e., $A_g(C_{2h})$], (c) an example of the E_g phonon (at approximately 240 cm^{-1}) intensity experiencing a clear discontinuity in the LR channel but remaining absent in the LL channel corresponding to an $E_g(C_{3i})$ phonon transforming into a $B_g(C_{2h})$ mode, and (d) M_2-mode intensity. Inset shows an enlargement between 1.5 and 2.5 T with both increasing ($+B$) and decreasing ($-B$) magnetic fields. Error bars correspond to one standard error of the fitted peak intensities. (e) Schematic illustration of the shearing of CrI_3 layers across the magnetic phase transition B_c. The light blue ellipses represent the directors between layers formed because of this lattice deformation.

on their broken time-reversal symmetry and thickness independence [15]. Here, we can immediately rule out the possibility that they are conventional bulk spin waves based on the magnetic field independence of their frequencies below B_c, and we can confidently associate them with the SAFM because of their disappearance above B_c. Based on this finding, we propose one possible origin of $M_{1,2}$ to

be a collective excitation made of two parts, one being the c-axis zone boundary phonon of the nonmagnetic lattice $A(\vec{k}_c, \omega)$ and the other being the layered AFM order $M(-\vec{k}_c, 0)$, where $\vec{k}_c$ is the out-of-plane wave vector for the constituent phonon (A) and magnetism (M) at frequencies of ω and 0 (i.e., elastic scattering off the layered AFM order), respectively. Such a collective excitation breaks the time-reversal symmetry, possesses a total momentum of zero, and becomes inaccessible in the FM phase above B_c due to the finite momenta (see detailed analysis in Supplemental Material Sec. 8 [23]). In other words, $M_{1,2}$ corresponds to a special zone folding by a single copy (or more precisely, an odd number of copies) of the magnetic order that breaks the time-reversal symmetry. However, this proposed origin cannot account for the thickness independence reported in Ref. [15]. Further experiments are needed to pin down the exact nature of both M_1 and M_2 modes. Nevertheless, they are good indicators for the SAFM state and the rhombohedral crystal lattice [Figs. 3(d) and 1(d)]. In contrast to conventional structural transitions, the emergence of this 3D quantum nematic order is driven by an external magnetic field that has a much stronger coupling to electrons than to ions, supporting an electronic origin for this structural transition. One natural mechanism for it could be that this interlayer shear deformation increases the distance between the nearest interlayer spins and thereby reduces the exchange energy penalty for the field-induced layered AFM-to-FM transition. Magnetic field-dependent Raman data on CrI_3 flakes show consistent results (see Supplemental Material Sec. 9 [23]).

D. Temperature vs magnetic field phase diagram

We now proceed to construct the temperature versus magnetic field phase diagram for bulk CrI_3 by performing temperature- (magnetic field-) dependent Raman measurements at multiple magnetic fields (temperatures). We show in Fig. 4(a) the temperature dependence of the M_{0c} FM frequency at a series of magnetic fields, and we clearly observe a crossover between FM and paramagnetic (PM) states at approximately 65 K at all applied magnetic fields [33,34]. This crossover is represented by the striped line with the experimental data points from this work in Fig. 4(c), and its extrapolation to zero magnetic field indeed corroborates the FM transition temperature of 61 K obtained from the magnetization measurements in 3D CrI_3 bulk [13]. Meanwhile, we display in Fig. 4(b) the magnetic field dependence of the M_2 intensity at several temperatures, and we discover a decreasing trend of the critical magnetic field B_c with increasing temperatures. This observation shows that the novel mixed state of SAFM and BFM in bulk CrI_3 is bounded by a line of phase transitions of both the layered AFM-to-FM and the rhombohedral-to-monoclinic structures, which is highlighted by a solid brown line in Fig. 4(c). Furthermore,
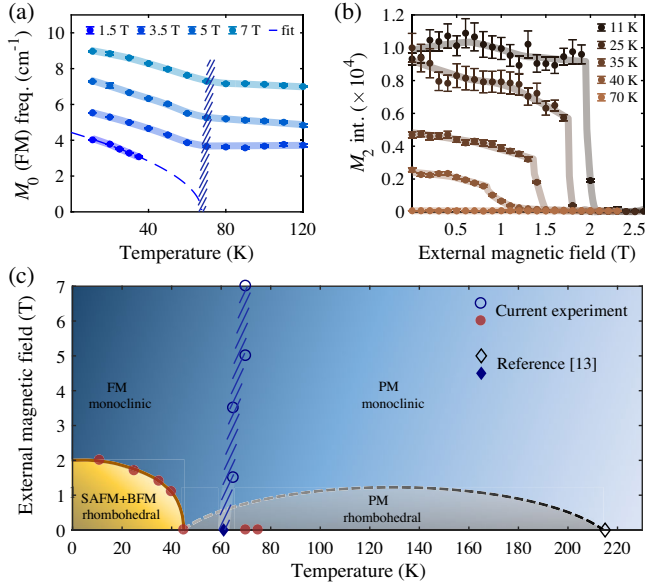
FIG. 4. Constructing the temperature vs external magnetic field phase diagram for 3D CrI_3. (a) Temperature dependence of the M_{0c} frequency for the FM spin-wave branch at multiple magnetic fields of 1.5 T (below B_c), 3.5, 5, and 7 T (above B_c). The dashed line is a fit to the data taken at 1.5 T, while the solid lines are guide to the eyes. The striped pattern highlights the crossover between the paramagnetism (PM) and ferromagnetism (FM). (b) Magnetic field dependence of the M_2 intensity at multiple temperatures of 11, 25, 35, 40 K (below T_c), and 70 K (above T_c). Error bars correspond to one standard error of the fitted parameters. (c) A temperature vs external magnetic phase diagram constructed based on both the findings from the current work (blue open and brown filled circles) and the literature (blue open and filled diamonds, Ref. [13]). The brown solid line represents a true phase boundary between the mixed magnetic phase with a rhombohedral structure and the FM phase with a monoclinic structure. The gray dashed line is for a potential phase boundary between the rhombohedral and monoclinic PM phases. The blue stripped pattern indicates the crossover between the PM and FM phases.

based on the fact that the crystal structure of 3D CrI_3 bulk transits from the rhombohedral to monoclinic symmetry across approximately 220 K from below at 0 T [13], we propose the presence of a phase boundary for the paramagnetic rhombohedral phase so as to connect the two regions of monoclinic structures above 220 K at $B = 0$ T and below 45 K at $B > B_c$. Please note that while the starting point of this phase boundary is determined to be at $T = 220$ K, $B = 0$ T, its end point is unknown due to a lack of experimental data, and thus, the gray dashed line in Fig. 4(c) presents only one possibility.

III. SUMMARY AND CONCLUSION

Our findings in 3D CrI_3 bulk of a novel mixed state of the surface-layered AFM and the bulk FM and a magnetic-field-induced first-order structural phase transition reveal a rich phase diagram for this VDW magnetic

semiconductor, which unambiguously resolves the puzzling evolution from the FM in 3D to the layered AFM in 2D CrI_3. Furthermore, controlling this unique magnetism in VDW magnets and its interplay with crystalline structures opens up new possibilities for the realization of novel 2D magnetic phases and the applications in modern spintronics. While a broader class of VDW magnets with such a unique magnetism and strong magnetoelastic coupling are to be identified, CrI_3 serves as an ideal platform to explore a variety of external controls, such as electric field, strain, and charge-carrier doping, on the magnetism and its interplay with other degrees of freedoms.

IV. METHODS

A. Growth of CrI_3 single crystals

Single crystals of CrI_3 are grown by the chemical-vapor-transport method. Chromium power (99.99% purity) and iodine flakes (99.999%) in a 1:3 molar ratio are put into a silicon tube with a length of 200 mm and an inner diameter of 14 mm. The tube is pumped down to 0.01 Pa and sealed under vacuum and then placed in a two-zone horizontal tube furnace. The two growth zones are raised slowly to 903 and 823 K for two days and are then held there for another seven days. Shiny, black, platelike crystals with lateral dimensions of up to several millimeters can be obtained from the growth. In order to avoid degradation, the CrI_3 crystals are stored in a nitrogen-filled glovebox and exfoliated in the dark to expose fresh surfaces right before the experiment (the air exposure time in a dark environment was less than 10 s before the sample is sealed in the cryostat vacuum chamber).

B. Micro-Raman spectroscopy

Micro-Raman spectroscopy measurements are carried out using a 632.81-nm excitation laser with a full width at half maximum of 0.85 cm^{-1} on resonance with the charge transfer and Cr^{3+} to $^4A_1$ transitions of CrI_3 in order to increase the Raman sensitivity. According to the absorption measurements taken in CrI_3 flakes, the optical penetration depth in CrI_3 for 633 nm is on the order of 30 layers. The laser beam on the sample site is focused down to approximately 3 μm in diameter, and the laser power is kept at 80 μW, which corresponds to a similar fluence used in the literature (10 μW over a 1-μm-diameter area) to minimize the local heating effect. Backscattering geometry is used. The scattered light is dispersed by a Horiba LabRAM HR Evolution Raman microscope (1800 groves/mm grating) from Horiba Scientific and detected by a thermoelectric cooled CCD camera provided by Horiba Scientific as well. Because of the small sample size on the order of a few microns, we use the confocal microscope geometry at a magnification of 40× to position the laser spot onto the sample of interest and perform a Raman spectroscopy experiment. In order

TABLE I. Transmission efficiency and their corresponding Stokes and anti-Stokes edges for the notch filter used in the experiment with a 632.81-nm excitation laser. The transmission efficiency is less than 10% in $[-1.8, 3.7]$ cm^{-1}, between 10% and 50% over the ranges of $[3.7, 4.2]$ and $[-2.2, -1.8]$ cm^{-1}, and between 50% and 90% over the ranges of $[4.2, 7.8]$ and $[-6.3, -2.2]$ cm^{-1}.

Transmission efficiency	Stokes edge (cm^{-1})	Anti-Stokes edge (cm^{-1})
10%	3.7	−1.8
50%	4.2	−2.2
90%	7.8	−6.3

to suppress the reflected light and Rayleigh scattering, we add a notch filter with a central wavelength of 632.85 nm, with its transmission profile described in Table I. A commercial variable temperature (<10–325 K), closed-cycle, microscopy cryostat from Cryo Industries of America, Inc. is interfaced with the Raman microscope. A commercial cryogen-free room-temperature-bore (2 in diameter and 6.88 in long) superconducting magnet from Cryo Industries of America, Inc. is used to achieve the variable out-of-plane magnetic field from 0 to 7 T. The cryostat cold finger, on which the samples are mounted, is inserted into the center of the room-temperature bore of the magnet. In this work, the selection rule measurements are performed mainly under the circularly polarized basis to eliminate any artifacts of the Faraday effect from the microscope objective subject to the strong stray magnetic field. All thermal cycles are performed at a base pressure lower than 7×10^{-7} torr.

S. L., Z. Y., and X. L. contributed equally to this work. L. Z. and R. H. conceived and initiated this project; S. T., C. L., and H. L. synthesized and characterized the bulk CrI$_3$ single crystals; Z. Y., G. Y., and R. H. performed the Raman measurements; S. L. performed the magnetic field-dependent spin-wave dispersion calculations under the guidance of K. S. and L. Z.; H. H. K., B. Y., and A. W. T. made the CrI$_3$ flake samples and performed magnetotunneling resistivity measurements. S. L., X. L., and L. Z. analyzed the data; S. L., X. L., R. H., and L. Z. wrote the manuscript, and all authors participated in the discussions of the results.

[1] C. Gong et al., *Discovery of Intrinsic Ferromagnetism in Two-Dimensional van der Waals Crystals*, Nature (London) **546**, 265 (2017).

[2] B. Huang et al., *Layer-Dependent Ferromagnetism in a van der Waals Crystal down to the Monolayer Limit*, Nature (London) **546**, 270 (2017).

[3] D. R. Klein et al., *Probing Magnetism in 2D van der Waals Crystalline Insulators via Electron Tunneling*, Science **360**, 1218 (2018).

[4] T. Song et al., *Giant Tunneling Magnetoresistance in Spin-Filter van der Waals Heterostructures*, Science **360**, 1214 (2018).

[5] H. H. Kim, B. Yang, T. Patel, F. Sfigakis, C. Li, S. Tian, H. Lei, and A. W. Tsen, *One Million Percent Tunnel Magnetoresistance in a Magnetic van der Waals Heterostructure*, Nano Lett. **18**, 4885 (2018).

[6] Z. Wang, I. Gutiérrez-Lezama, N. Ubrig, M. Kroner, M. Gibertini, T. Taniguchi, K. Watanabe, A. Imamoğlu, E. Giannini, and A. F. Morpurgo, *Very Large Tunneling Magnetoresistance in Layered Magnetic Semiconductor* CrI$_3$, Nat. Commun. **9**, 2516 (2018).

[7] J.-U. Lee, S. Lee, J. H. Ryoo, S. Kang, T. Y. Kim, P. Kim, C.-H. Park, J.-G. Park, and H. Cheong, *Ising-Type Magnetic Ordering in Atomically Thin* FePS$_3$, Nano Lett. **16**, 7433 (2016).

[8] K. Kim et al., *Antiferromagnetic Ordering in van der Waals 2D Magnetic Material* MnPS$_3$ *Probed by Raman Spectroscopy*, 2D Mater. **6**, 041001 (2019).

[9] K. Kim, S. Y. Lim, J.-U. Lee, S. Lee, T. Y. Kim, K. Park, G. S. Jeon, C.-H. Park, J.-G. Park, and H. Cheong, *Suppression of Magnetic Ordering in XXZ-Type Antiferromagnetic Monolayer* NiPS$_3$, Nat. Commun. **10**, 345 (2019).

[10] S. Jiang, J. Shan, and K. F. Mak, *Electric-Field Switching of Two-Dimensional van der Waals Magnets*, Nat. Mater. **17**, 406 (2018).

[11] B. Huang et al., *Electrical Control of 2D Magnetism in Bilayer* CrI$_3$, Nat. Nanotechnol. **13**, 544 (2018).

[12] S. Jiang, L. Li, Z. Wang, K. F. Mak, and J. Shan, *Controlling Magnetism in 2D* CrI$_3$ *by Electrostatic Doping*, Nat. Nanotechnol. **13**, 549 (2018).

[13] M. A. McGuire, H. Dixit, V. R. Cooper, and B. C. Sales, *Coupling of Crystal Structure and Magnetism in the Layered, Ferromagnetic Insulator* CrI$_3$, Chem. Mater. **27**, 612 (2015).

[14] L. Chen, J. H. Chung, B. Gao, T. Chen, M. B. Stone, A. I. Kolesnikov, Q. Huang, and P. Dai, *Topological Spin Excitations in Honeycomb Ferromagnet* CrI_3, Phys. Rev. X **8**, 041028 (2018).

[15] W. Jin *et al.*, *Raman Fingerprint of Two Terahertz Spin Wave Branches in a Two-Dimensional Honeycomb Ising Ferromagnet*, Nat. Commun. **9**, 5122 (2018).

[16] K. L. Seyler *et al.*, *Ligand-Field Helical Luminescence in a 2D Ferromagnetic Insulator*, Nat. Phys. **14**, 277 (2018).

[17] P. A. Fleury and R. Loudon, *Scattering of Light by One- and Two-Magnon Excitations*, Phys. Rev. **166**, 514 (1968).

[18] W. Hayes and R. Loudon, *Scattering of Light by Crystals* (Dover Publication, New York, 2012).

[19] B. Huang, J. Cenker, X. Zhang, E. L. Ray, T. Song, T. Taniguchi, K. Watanabe, M. A. McGuire, D. Xiao, and X. Xu, *Tuning Inelastic Light Scattering via Symmetry Control in the Two-Dimensional Magnet* CrI_3, Nat. Nanotechnol., **15**, 212 (2020).

[20] A. McCreary *et al.*, *Distinct Magneto-Raman Signatures of Spin-Flip Phase Transitions in* CrI_3, arXiv:1910.01237.

[21] Y. Zhang *et al.*, *Magnetic Order-Induced Polarization Anomaly of Raman Scattering in 2D Magnet* CrI_3, Nano Lett. **20**, 729 (2020).

[22] J. Ji, A. Zhang, J. Fan, Y. Li, X. Wang, J. Zhang, E. W. Plummer, and Q. Zhang, *Giant Magneto-Optical Raman Effect in a Layered Transition Metal Compound*, Proc. Natl. Acad. Sci. U.S.A. **113**, 2349 (2016).

[23] See Supplemental Material at http://link.aps.org/supplemental/10.1103/PhysRevX.10.011075 for additional information for Raman selection rules in the circular polarization basis, magnetic field-dependent Raman spectra taken in different polarization channels and on samples of different thicknesses, magnetization measurement results, and spin wave calculations.

[24] D. Shcherbakov *et al.*, *Raman Spectroscopy, Photocatalytic Degradation, and Stabilization of Atomically Thin Chromium Tri-Iodide*, Nano Lett. **18**, 4214 (2018).

[25] S. Djurdjić-Mijin, A. Solajic, J. Pesic, M. Scepanovic, Y. Liu, A. Baum, C. Petrovic, N. Lazarevic, and Z. V. Popovic, *Lattice Dynamics and Phase Transition in* CrI_3 *Single Crystals*, Phys. Rev. B **98**, 104307 (2018).

[26] L. Webster, L. Liang, and J.-A. Yan, *Distinct Spin-Lattice and Spin-Phonon Interactions in Monolayer Magnetic* CrI_3, Phys. Chem. Chem. Phys. **20**, 23546 (2018).

[27] D. T. Larson and E. Kaxiras, *Raman Spectrum of* CrI_3: *An Ab Initio Study*, Phys. Rev. B **98**, 085406 (2018).

[28] N. W. Ashcroft and N. D. Mermin, *Solid State Physics* (Holt, Rinehart and Winston, New York, 1976).

[29] J. C. Tolédano and P. Tolédano, in *Magnetic and Liquid Crystal Systems* (World Scientific, Singapore 1987).

[30] B. Niu *et al.*, *Coexistence of Magnetic Orders in Two-Dimensional Magnet* CrI_3, Nano Lett. **20**, 553 (2020).

[31] D. C. Johnston, *Magnetic Dipole Interactions in Crystals*, Phys. Rev. B **93**, 014421 (2016).

[32] N. Sivadas, S. Okamoto, X. Xu, C. J. Fennie, and D. Xiao, *Stacking-Dependent Magnetism in Bilayer* CrI_3, Nano Lett. **18**, 7658 (2018).

[33] P. M. Chaikin and T. C. Lubensky, *Principles of Condensed Matter Physics* (Cambridge University Press, Cambridge, England, 2000).

[34] J. Cardy, P. Goddard, and J. Yeomans, *Scaling and Renormalization in Statistical Physics* (Cambridge University Press, Cambridge, England, 1996).